Journal of Atmospheric and Solar–Terrestrial Physics 218 (2021) 105627

Contents lists available at ScienceDirect

Journal of Atmospheric and Solar-Terrestrial Physics

journal homepage: www.elsevier.com/locate/jastp

Characteristics of a mesospheric front observed in Polar Mesospheric Cloud fields

Brentha Thurairajah [a,*], Chihoko Y. Cullens [b], Scott M. Bailey [a]

[a] Center for Space Science and Engineering Research, Bradley Department of Electrical and Computer Engineering, Virginia Tech, Blacksburg, VA, USA
[b] Space Science Laboratory, University of California, Berkeley, CA, USA

ARTICLE INFO

Keywords:
polar Mesospheric clouds
Mesospheric inversion layer
Gravity waves

ABSTRACT

We report on a Polar Mesospheric Cloud (PMC) front structure observed on July 2, 2007 over Greenland. This structure appears to be localized solitary wave, with a sharp boundary that separates a cloud and cloud-free region. Near-coincident temperature measurements indicate a 20 K temperature difference between these two regions that likely contributed to the sharp PMC front boundary. Gravity wave (GW) temperature amplitude and buoyancy frequency show that large amplitude GWs and the formation of a stable atmospheric layer between two unstable regions supported the formation of a pronounced mesospheric temperature inversion that destroyed PMCs. Given the absence of an inversion layer close to the location of PMC front, it is not clear if a similar thermal duct but with colder temperatures supported the formation of a single wave resulting in the formation of the observed PMC front. The buoyancy frequency structure with stable and unstable regions also indicates mesospheric wave propagation, and is present in both the cloud and cloud-free regions. We identify a tropospheric low-pressure area and a frontal system as potential sources of these mesospheric GWs. Ray-tracing simulations indicate that GWs from these sources propagated to the mesosphere and may have contributed to the observed PMC variability.

1. Introduction

Polar Mesospheric Clouds (PMCs) typically occur in the high-latitude summer mesosphere, but have also been reported at mid-latitudes (Stevens et al., 2009; Russell et al., 2014). In addition to the more frequent observations of PMCs at mid-latitudes, in recent years PMCs have also been reported at low latitudes, as low as 34.1 °N (Phillips, 2019). While these changes may or may not suggest a link to climate change (Thomas, 2003; von Zahn, 2003), these clouds at the edge of space (~82–86 km) provide information regarding the mesospheric environment. PMC variability has led to studies on inter-hemispheric teleconnections (e.g. Karlsson et al., 2009), lower atmospheric coupling (e.g. Yue et al., 2014), planetary waves (e.g. France et al., 2018), tides (e.g. Stevens et al., 2017), gravity waves (e.g. Chandran et al., 2012; Dalin et al., 2016), and long-term trends in the summer mesosphere (e.g. Dalin et al., 2020).

PMCs exhibit complex spatial structures but have also revealed several unique morphological forms including the four main types (Veils, Bands, Billows, Whirls) and other structures such as ice voids, fronts, bores, and vortex like structures (e.g. Dalin et al., 2013; Thurairajah et al., 2013; Megner et al., 2018; Fritts et al., 2020). These structures that are generally signatures of atmospheric gravity waves (GWs), turbulence, and/or Kelvin Helmholtz instability provide important clues to the dynamic processes that control the summer mesospheric region. While GW band structures are ubiquitous in mesospheric cloud fields (e.g. Dalin et al., 2004; Chandran et al., 2009), in this study we focus on a mesospheric front structure in PMCs, which we define as a solitary wave (i.e. a single wave with a wave crest) or a sharp step-like boundary that separates a mesospheric cloud and a no cloud region. We refer to this structure as a 'front' based on the terminology used in tropospheric weather systems i.e. cold or warm front that separate air masses with different density or temperature.

Fronts in mesospheric clouds have been observed by ground-based cameras (Dubietis et al., 2011; Dalin et al., 2013), and from space by the Cloud Imaging and Particle Size (CIPS) experiment on the Aeronomy of Ice in the Mesosphere (AIM) satellite (Thurairajah et al., 2013). Dubietis et al. (2011) presented a case study of a localized quasi-stationary single wave event over Lithuania (55°N, 26°E). The wave observed for ~30 min by a ground-based camera was found to be moving in the north-northwest direction with an average speed of 5.0 ±

* Corresponding author.
E-mail address: brenthat@vt.edu (B. Thurairajah).

https://doi.org/10.1016/j.jastp.2021.105627
Received 10 November 2020; Received in revised form 15 March 2021; Accepted 16 March 2021
Available online 25 March 2021
1364-6826/

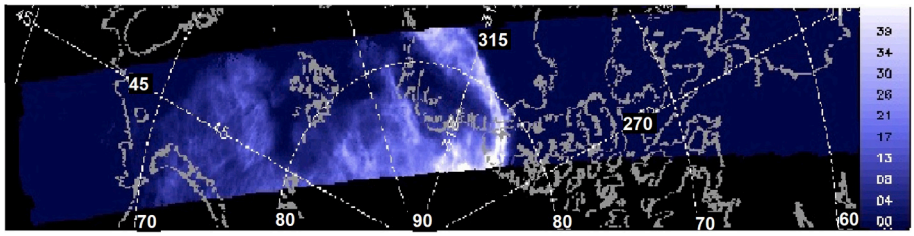

Fig. 1. CIPS PMC image in an orbital swath obtained on July 2, 2007 (orbit 1013). The albedo color bar range is from 00 (dark blue) to $> 39.0 \times 10^{-6}$ (white) sr^{-1}.

1.7 m/s with respect to the ground. The authors noted that this slow speed created an illusion of a stationary wave. Using data from 18 such events, Dubietis et al. reported that these quasi-stationary waves had lengths varying from 50 to 450 km and lasted for 25–55 min. Dalin et al. (2013) presented a case study of a common volume ground-based and space measurement of a mesospheric front over Canada (55°N, 113°W). The visual horizontal extension of the front was 322 km and was observed to be moving at a ground speed of 31.1 m/s in the northwest direction. Common volume temperature observations from the SABER (Sounding of the Atmosphere using Broadband Emission Radiometry) instrument on NASA's TIMED (Thermosphere Ionosphere Mesosphere Energetics Dynamics) satellite in the cloud area and in the cloud free area showed a temperature difference of 20–25 K at 84–85.6 km. Thus, across the visual boundary of the mesospheric front, Dalin et al. reported a meridional temperature gradient of 0.07 K/km at 85 km. Thurairajah et al. (2013) identified front structures using CIPS PMC images from 2007 to 2011. Using visual identification, 9 fronts were observed in July of Northern Hemisphere (NH) 2007–2010 and 13 fronts in January of Southern Hemisphere (SH) 2008/2009–2010/2011 PMC seasons. The front on July 2, 2007 over Greenland (~80°N, 50°W) was observed over three consecutive images, with the sharp boundary starting to deteriorate in the second and third images. This feature was reported to be moving at a speed of 60 m/s and given the 90 min cadence between successive CIPS images, was reported to have a lifetime of at least 90 min.

The above reports on PMC fronts are similar to mesospheric frontal events observed in OH airglow layers in the upper mesosphere (~90–100 km) (Brown et al., 2004; Pautet et al., 2018 and references therein). These mesospheric fronts in airglow images are classified as mesospheric bores or wall events based on the physical structure (Dewan and Picard, 1998). The mesospheric bore observed in airglow images is defined as a propagating sharp front that is usually followed by a wave train (known as an undular bore) or turbulence (known as turbulent bore) (Yue et al., 2010). It is understood that mesospheric bores can form and propagate due to an inversion layer (thermal duct) and/or a large wind shear (Doppler duct) in the mesopause region that forms a duct for bore propagation (Taylor et al., 1995; Dewan and Picard, 1998; Smith et al., 2005; She et al., 2004; Simkhada et al., 2009). These ducts support horizontal wave propagation and can form due to the forcing generated by the critical level interaction between GW and mean winds (Dewan and Picard, 2001). A wall event in airglow images appears as a dark or bright sharp front with trailing crests that have a phase shift with altitude, but is not ducted like mesospheric bore events (Swenson and Espy, 1995; Smith, 2014).

Previous studies of PMC fronts have focused mainly on visual characteristics like the spatial extent of the dominant wave and the direction of propagation. To our knowledge, only Dalin et al. (2013) have reported on the presence of a significant temperature gradient across the boundary of an observed PMC front separating cloud and cloud-free regions. Given the visual similarity between PMC fronts and mesospheric bores observed at a higher altitude (~90–100 km) in airglow images, a more detailed analysis of these structures may provide clues to the summer mesospheric dynamical processes that support their formation. In this paper, we present a detailed case study of a mesospheric front observed on July 2, 2007 by the CIPS instrument. We analyze the mesospheric environment surrounding this front using co-located SABER data. We analyze the background temperature structure, atmospheric stability, and GW amplitude, and any similarities to mesospheric bores. GW ray-tracing experiments are used to identify potential tropospheric GW sources, their propagation to the mesosphere, and their role in the observed PMC variability.

2. Observations and analysis

2.1. PMC front observed by CIPS/AIM

CIPS is an UV panoramic imager (McClintock et al., 2009; Russell et al., 2009) that uses four cameras to image the atmospheric and PMC radiance in the latitude range of ~40–85°N during the summer. PMC data in 2007 are reported in terms of cloud albedo, ice water content, and particle size at a horizontal resolution of 25 km^2 (Lumpe et al., 2013). CIPS images map nearly the entire polar cap with 15-orbits per day leading to multiple coverage of a single location. The CIPS cloud data have been validated against data from the Solar Backscatter Ultraviolet (SBUV) instruments and have been found to be appropriate for science studies (Benze et al., 2009, 2011). Fig. 1 shows the CIPS albedo image for orbit 1013 on July 2, 2007. Albedo is defined as the ratio of the scattered radiance to the incoming solar irradiance (Rusch et al., 2009;

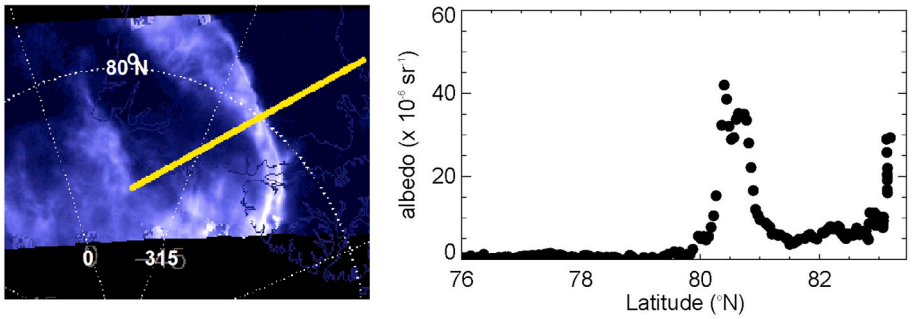

Fig. 2. (left panel) A larger cropped version of the PMC front shown in Fig. 1. The yellow line indicates a scan across the boundary of the front. (right panel) The albedo values across the scan as a function of latitude.

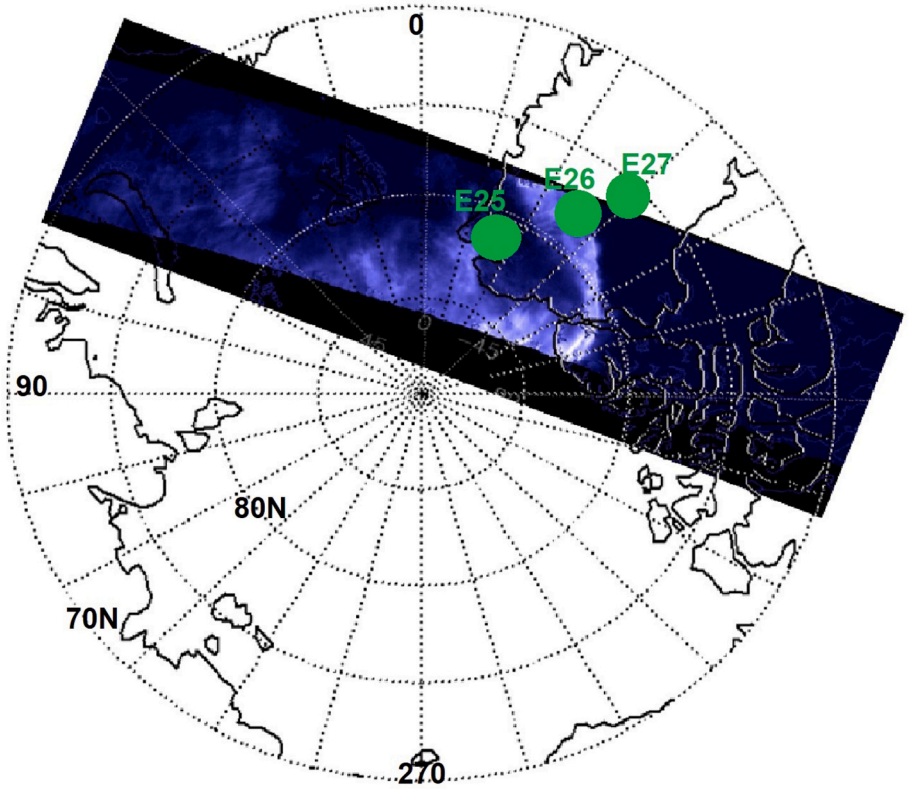

Fig. 3. Global perspective of the location of the front observed by CIPS. Green dots denote the SABER observation events E25, E26, and E27.

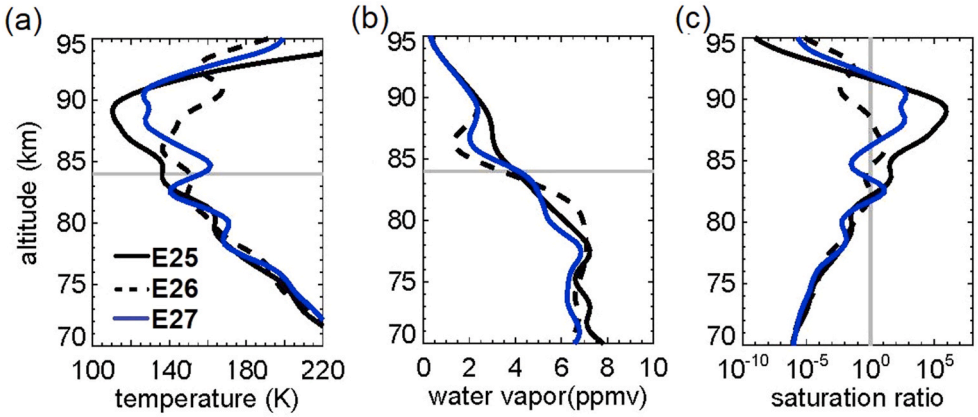

Fig. 4. SABER (a) Temperature (b) water vapor and (c) saturation ratio, S profiles for events E25 (solid black), E26 (dashed), and E27 (solid blue) across the boundary of the PMC front. Grey horizontal line in (a) and (b) is at 84 km. Grey vertical line in (c) is at S = 1.

Bailey et al., 2009). A PMC front is observed over Greenland at 19:14 UT and extends across the 900 km width of the CIPS orbit. No trailing waves are observed behind what appears to be a solitary wave. A cropped version focusing on the PMC front and the albedo values from a scan across the front structure is shown in Fig. 2. The PMC front shows a step-function in albedo i.e. a sharp boundary between cloud and cloud-free region. Between 80° and 80.5° latitude, the albedo decreases from a high of ~42 × 10^{-6} sr^{-1} to less than 5 × 10^{-6} sr^{-1}.

2.2. Temperature and water vapor from SABER/TIMED

SABER is a limb-scanning infrared radiometer that measures global pressure, temperature, water vapor, geopotential height, and trace species from ~10 to 110 km (Russell et al., 1999). SABER temperatures are retrieved from the limb radiance in the 15 μm CO_2 band and water vapor volume mixing ratios (VMRs) are retrieved from the limb radiances in the 6.3–7.3 μm spectral region. SABER temperature and water vapor have been validated by Remsberg et al. (2008) and Rong et al. (2019), respectively and are available at a vertical grid of 0.4 km. The temperature random errors are 1.4 K at 80 km and 3.3 K at 90 km. On July 2, 2007, three SABER events in orbit 30141 provide near-coincident temperature and water vapor observations across the boundary of the mesospheric front. These three closest observations to the PMC front occurred ~40 min after the CIPS observation. Fig. 3 shows a global map with the location of the front observed by CIPS on July 2, 2007 (19:14 UT) and the location of the measurements made by SABER events E25, E26, and E27 at 19:52 UT, 19:53 UT, and 19:54 UT, respectively. These events span across the front and provide temperature and water vapor data in the cloud and cloud-free regions. The approximate distance between E25 and E26 locations is 454 km, and between E26 and E27 is

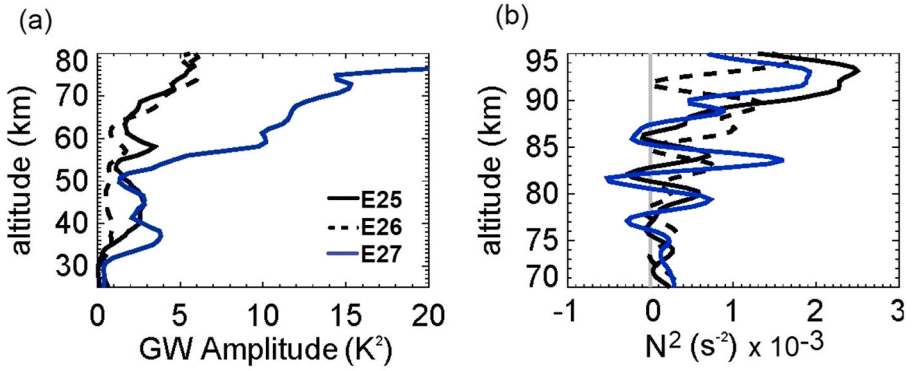

Fig. 5. (a) GW squared temperature amplitude and (b) Buoyancy frequency squared for events E25 (solid black), E26 (dashed), and E27 (solid blue) across the boundary of the PMC front. The vertical grey line in (b) indicates $N^2 = 0$. Note that the y-axis is different in (a) and (b).

268 km. Since SABER is a limb-viewing instrument, each SABER observation is an average over an along track span of about 200 km or ~2°.

Fig. 4a and b shows the temperature and water vapor profiles in the cloud-free region (E27), over the location of the front (E26), and the cloud region to the left of the front (E25). Even with the estimated movement of 60 m/s of this front structure, we assume that the profiles measured by E27 and E25 represent the temperature and water vapor in the cloud and cloud-free regions. Fig. 4a indicates that there is a pronounced mesospheric inversion layer (MIL) in the cloud-free region, a "normal" summertime temperature profile with a small non-significant enhancement in the cloud region, and a similar small temperature enhancement in between these two profiles. Following the definitions from Irving et al. (2014), the MIL in the upper mesosphere in event E27 has the following characteristics-

- Peak altitude = 84.7 km
- Amplitude (T_{max}-T_{min}) = 20.8
- Depth (Z_{max} – Z_{min}) = 1.9
- Bottom side T gradient = 10.9 K/km
- Top side lapse rate = - 8K/km

Fig. 4a also shows that a temperature difference of 20 K separates the two different air masses (i.e. clouds, no-clouds). For example, the temperature at 84 km in the cloud (E25) region is 136 K and the temperature in the cloud-free region (E27) is 156 K. This result is similar to that reported by Dalin et al. (2013) where they concluded that this temperature difference was responsible for the front jump separating the area with and without mesospheric clouds. The water vapor profiles (Fig. 4b) indicate that at 84 km both the cloud and cloud-free regions have similar values of ~4.0 ppmv. PMCs form under conditions of cold temperatures and enhanced water vapor and exist when the saturation ratio (S) is much greater than one (i.e. supersaturated state). S is defined as the ratio of water vapor partial pressure (P_{H2O}) and saturation vapor pressure (P_{SAT}). From Murphy and Koop (2005), for a temperature T, P_{SAT} is defined as,

$$\log(P_{SAT}) = 9.550426 - \frac{5723.265}{T} + 3.53068 logT - 0.007238232T \qquad \text{(Pa)}$$

Fig. 4c shows the vertical profiles of S for events E25, E26, and E27. PMCs can form when $P_{SAT} < 1.0 \times 10^{-8}$ hPa (low saturation vapor pressure; T < 145 K) and $P_{H2O} > 1.0 \times 10^{-8}$ hPa (high water vapor partial pressure; H_2O > 1.0 ppmv) (Rong et al., 2012). Thus the mesosphere at a temperature of 136 K and water vapor mixing ratio of 4 ppmv will be super saturated ($S \gg 1$) and the mesosphere at a temperature of 156 K and water vapor mixing ratio of 4 ppmv will not be saturated ($S < 1$). This confirms that even with a time difference of 40 min between PMC and SABER observations, SABER was indeed observing cloud and cloud-free regions at 84 km in events 25 and 27, respectively.

Between these two profiles, for SABER observation event E26, the temperature and water vapor at 84 km were 151 K and 3.5 ppmv, respectively. These conditions do not support the formation of PMCs ($S < 1$) and we believe that the front structure has moved to the left of the location of E26 shown in Fig. 3. However, since SABER makes limb observations, CIPS would still see PMCs at these warm temperatures if the clouds were in a wave trough along a 200 km limb path. At 86 km, more humid conditions exist over the cloud region (3.1 ppmv) compared to the cloud-free region (2.1 ppmv). Between these two regions there is drier and lower water vapor value of 1.3 ppmv. The temperature at 86 km for all three events is < 145 K indicating that the mesospheric conditions at 86 km could have supported the formation of PMCs. However, as noted by Dalin et al. (2013), the warmer temperatures in the cloud-free region at the lower altitudes will have sublimated the falling ice particles leading to higher water vapor concentration. Since the growth time for the reformation of ice particles is much longer than sublimation (Dalin et al., 2013; Gadsden and Schröder, 1989) no PMCs will exist at these warmer temperatures. At 82 km, $S \approx 1$ for E25 and E26 and will not support the existence of PMCs. For E27, even though $S > 1$, the warmer temperatures at 84 km would not have allowed any ice particles to sediment down to 82 km.

3. Gravity wave activity

Temperature data from limb-viewing instruments such as SABER have been shown to be reliable for GW studies (e.g. Preusse et al., 2009; Ern et al., 2011; Yamashita et al., 2013; Thurairajah et al., 2017; Ern et al., 2018 and references therein). Here we summarize the method to derive GW temperature amplitude from SABER. Perturbation temperature profiles are calculated by subtracting the background temperature profile, which is the sum of the zonal mean component (wavenumber 0) and planetary wave components (wavenumbers 1–5). A wavelet analysis is applied to the perturbation profiles to calculate three dominant vertical wavelengths. These wavelengths are then used in a harmonic fit (20 km sliding windows) to calculate the GW temperature amplitude. A detailed explanation of the methodology can be found in for example Thurairajah et al. (2017) and references therein. Due to its observation filter, in the vertical wavelength range between 4 and 30 km, and depending on the distance between two profiles, SABER can be sensitive to GWs with horizontal wavelengths >100 km.

Fig. 5 shows the calculated GW squared temperature amplitude ($\widehat{T}^2$) in the stratosphere and mesosphere and Buoyancy frequency squared (N^2) in the upper mesosphere during the three SABER observation events. The GW temperature amplitude (Fig. 5a) is shown for the stratosphere and mesosphere from 25 to 80 km. Although SABER temperatures are available from ~15 to 110 km, this shortened altitude range is due to the 20 km sliding window used in the harmonic fits and

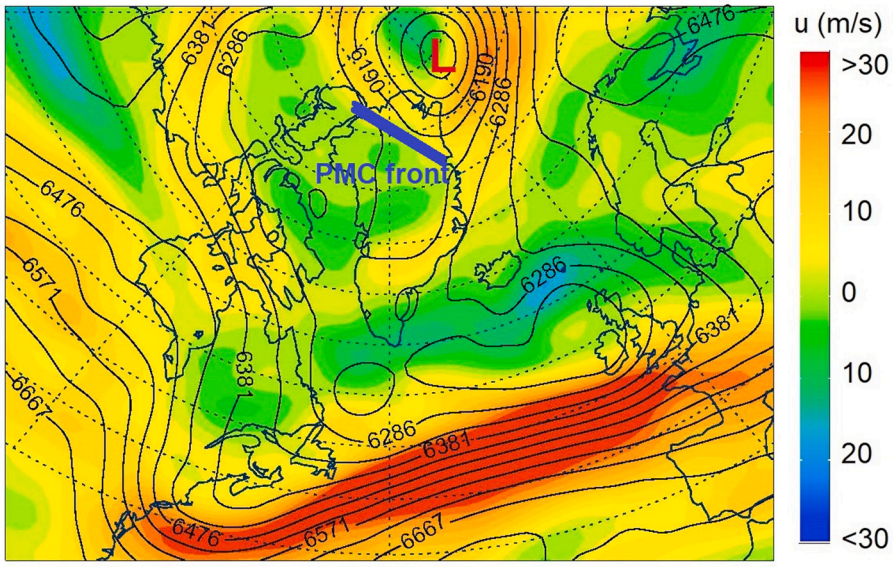

Fig. 6. 450 hPa level map of geopotential height (line contour) in units of meters and zonal wind (colored contour) on July 2, 2007 at 18:00 UT. The letter "L' denotes the low-pressure system over north-west Greenland. The approximate location of the PMC front is also shown.

the fact that the presence of MILs can introduce large errors in the perturbation temperature calculations. The GW amplitude increases exponentially with altitude for all three events, with a larger increase in the cloud-free region (E27). For example, at 75 km, the GW squared amplitude in the cloud-free region (E27) is 14.5 K^2 compared to 5.8 K^2 in the cloud region (E25). Previous studies on the influence of mesospheric GWs on PMCs have reported both a negative correlation between GW occurrence and PMC occurrence (Chandran et al., 2009), and a positive correlation between GW amplitude and PMC ice water content (Thurairajah et al., 2020). Moreover, Wilms et al. (2013) have reported no correlation between GW kinetic energy and PMC occurrence. While many factors such as the spectrum of GWs and location (e.g. PMC at mid-latitudes may have been advected from high-latitudes and thus are not influenced by local GWs) play a role in the effect of GWs on PMCs, in this study, the higher GW amplitude in the cloud-free region may have supported the formation of the MIL (e.g. Fritts et al., 2018) leading to warmer temperatures and the destruction of PMCs.

The buoyancy frequency squared in the mesosphere (Fig. 5b) in both the cloud and cloud-free regions shows wave like structure with vertical wavelength of ~6 km indicating wave propagation through the mesosphere. N^2 is positive (stable layer) at the altitude of 84 km (where PMCs typically occur), but is negative below and above this region indicating statically unstable regions. This structure has been shown to be favorable for bore propagation (Hozumi et al., 2018). The pronounced MIL with the warmer temperatures likely destroyed PMCs. In the cloud region, although the N^2 structure may have supported the reflection of wave energy into a thermal duct that lead to the formation of the PMC front, the co-located temperature profile does not show a significant MIL (i.e. the small temperature enhancement is within the SABER temperature measurement error). We would need temperature and wind measurements (large wind shears act as Doppler duct and may also support the formation of fronts) at the exact location and time of formation of the PMC front to verify if a thermal and/or Doppler duct is indeed responsible for the formation of PMC fronts.

4. Tropospheric GW source and vertical propagation paths

Since GWs play an important role in influencing the mesospheric environment, we investigate possible mesospheric GW sources in the lower atmosphere using tropospheric wind and geopotential height data. We also study the GW propagation paths using the Gravity-wave Regional Or Global Ray Tracer (GROGRAT) ray-tracing model. The GROGRAT ray-tracing model (Marks and Eckermann, 1995; Eckermann and Marks, 1997) provides GW propagation direction from the troposphere to the mesosphere (e.g. Preusse et al., 2009; Yamashita et al., 2013; Kalisch et al., 2014). The ray tracing equations take into account refraction of the wave vector due to vertical and horizontal gradients of the background atmosphere and includes meridional gradients of the Coriolis force. To identify tropospheric GW sources and for the ray-tracing simulations, we use winds, geopotential height, and temperature from the Navy Operational Global Atmospheric Prediction System –Advanced Level Physics (NOGAPS-ALPHA) model. This forecast/analysis model (Eckermann et al., 2009; Hoppel et al., 2008) assimilates data from the SABER and MLS instruments and provides a synoptic analysis of the atmosphere from 1000 to 0.01 hPa (~0–92 km). NOGAPS-ALPHA output is 6-hr global analysis fields at a spatial resolution of 2.25° latitude x 2.25° longitude.

Gerrard et al. (2004) have shown that tropospheric maps can be used to infer low-level disturbances like tropospheric jets that can be directly correlated to the occurrence of mesospheric clouds. Dalin et al. (2015) used NLC observations and reverse ray-tracing model studies to demonstrate the connection between a tropospheric occluded front and the appearance of an NLC layer with propagating internal GWs. More recently, Solodonovik et al. (2020) used weather maps to show that tropospheric factors such as the movement of cyclones and cold fronts influence the appearance and formation of NLCs. Solodovnik et al. correlated PMC fields to tropospheric weather systems and concluded that the positive correlation may be due to the propagation of internal GWs that support PMC formation. Following these studies, Fig. 6 shows the NOGAPS-ALPHA geopotential height and zonal winds on July 2, 2007 at 450 hPa (~6 km) in the area surrounding the location of the mesospheric PMC front. A low-pressure cell is present over the northwestern tip of Greenland, to the right of the location of the PMC front. Additionally, a tropospheric frontal system is present to the south of Greenland over 40–50°N. On top of this front, near the tropopause sits the polar jet with strong upper-level winds (not shown). The low pressure cell and the polar front jet are known sources of GWs (Fritts and Alexander, 2003) and persist through the day on July 2, 2007. In addition, the surface flow over the terrain of Greenland is a source of orographic GWs and Greenland is a known "hotspot" for GW generation (e.g. Hoffmann et al., 2013).

To analyze if GWs from these three sources reach the mesosphere,

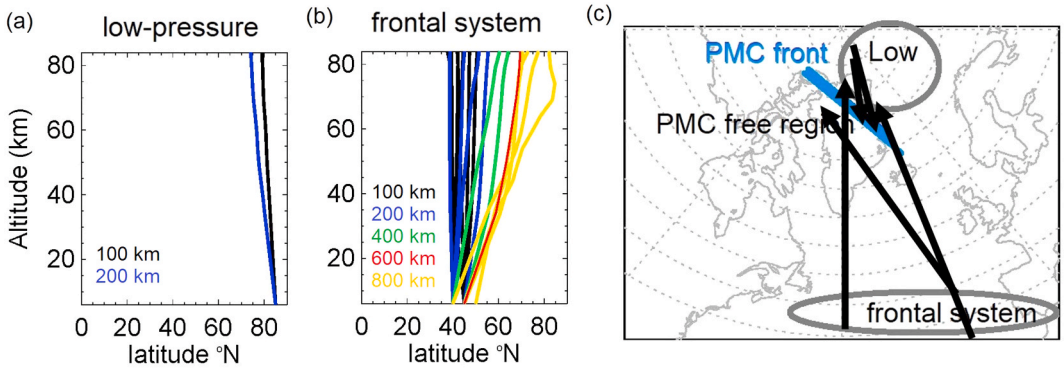

Fig. 7. (a, b) Ray-paths as a function of latitude and altitude for GWs launched from the area of the (a) tropospheric low and (b) tropospheric frontal system and reached 270–360°E longitude in the mesosphere. (c) A latitude longitude map indicating the location of the PMC front (blue), the tropospheric GW sources (low, frontal system) and the associated GW ray-paths (black arrows). The colors (black, blue, green, red, yellow) in (a) and (b) indicate the horizontal wavelengths of 100, 200, 400, 600 and 800 km, respectively.

GROGRAT simulations were performed by launching waves with horizontal wavelengths ≥100 km (λ_H = 100, 200, 400, 600, 800, 1000, and 1200 km) and ground-based horizontal phase speeds (c) of 0 m/s (orographic waves) and 20, 40 and 60 m/s (non-orographic waves). The waves were launched at 5° latitude and 10° longitude intervals from an altitude of 6 km on July 2, 2007. The waves were allowed to propagate for ~1 day until they dissipated or reached the PMC altitude (84 km). The simulations indicate that the background conditions were not favorable for the propagation of orographic waves (c = 0 m/s) to the mesosphere. Most waves with ground-based phase speed of 20 m/s also did not reach the vicinity of the PMC front at ~65–85°N, 270–360°E.

Fig. 7a shows the ray-paths from the tropospheric low pressure system (>75°N) that reached the mesosphere around the PMC front location (~65–85°N, 270–360°E) for c = 40 m/s. Fig. 7b shows the ray-paths from the tropospheric frontal system (~40–50°N, 270–360°E) that reached the mesosphere between 40 and 90°N, 270–360°E (i.e. same longitudes as the PMC front location) for c = 40 m/s. The ray-paths for c = 60 m/s were similar to 40 m/s and are therefore not shown. The waves from the tropospheric low that reach the PMC front location are of shorter wavelengths with λ_H = 100–200 km. The majority of the waves from the tropospheric frontal system (40–50°N) stay within this mid-latitude boundary in the mesosphere with a few longer wavelength waves (λ_H = 600–800 km) reaching the PMC front location. These wavelengths from tropospheric GW sources are in general agreement with previous modelling studies, where for example Gerrard et al. (2004) showed that GWs with $\lambda_H \approx$ 350 km can propagate from tropospheric lows to mesospheric altitudes, and O'Sullivan and Dunkerton (1995) showed that the horizontal wavelength of jet-generated GWs can vary from 600 to 1000 km. CIPS PMC images have also revealed mesospheric GWs with dominant horizontal wavelengths varying from 10 to 2000 km (Chandran et al., 2010; Zhao et al., 2015). Given the narrow PMC front structure, the coarse model resolution, and the fact that if the PMC front is indeed a ducted wave then the wave could have been short lived and/or travelled 1000s of km, we cannot directly relate the tropospheric GW sources to the formation of the PMC front. However, numerous studies have shown the vertical coupling between the troposphere and mesosphere via GWs. Given that these waves do reach PMC altitudes we believe that at least some of these waves may have been responsible for the formation of the MIL and are partly responsible for the PMC variability observed on this day. Fig. 7c shows a latitude longitude plot summarizing the ray paths from the two tropospheric GW sources to the location around the PMC front.

5. Summary

We reported on a PMC front structure observed by the CIPS instrument on July 2, 2007 over Greenland. This PMC front appears as a solitary wave and has a sharp boundary that separates cloud and cloud-free regions. Near-coincident temperature measurements across the PMC front boundary from SABER indicate a pronounced MIL in the cloud-free region. In the PMC region and close to the location of the front a small temperature enhancement is observed. Simultaneous water vapor measurements confirm that the cloud region is supersaturated supporting the formation of PMCs compared to the cloud-free region. The large temperature difference (20 K) between the cloud and cloud-free regions contributed to the sharp boundary at the PMC front. We calculated the GW amplitude and buoyancy frequency from SABER temperatures. The GW amplitude is larger in the cloud-free region compared to the cloud region. The buoyancy frequency in the mesosphere indicates vertical wave propagation and alternate layers of unstable and stable regions that support the formation of thermal ducts or inversion layers where a localized single wave can form. Thus, while the pronounced MIL destroyed PMCs leading to the cloud-free region, there is a possibility that a similar thermal duct in the PMC region lead to the formation of the PMC front. Coincident temperature and wind measurements are needed to verify this hypothesis. On July 2, 2007, tropospheric synoptic maps indicate persistent tropospheric weather systems (low-pressure cell, frontal systems) that are known GW sources. A ray-tracing simulation from these tropospheric GW sources indicate that some GWs reach the area near the PMC front. While we can only speculate that some of these waves that reached the upper mesosphere contributed to the formation of the MIL that may have supported a PMC front as a ducted wave or perhaps led to the observed cloud-free region, a higher resolution model that can include smaller horizontal wavelengths (i.e. < 100 km) could provide a more detailed look at the GW dynamics that support various PMC structures. Along with these model results, more observational studies with a significant number of coincident front and temperature/wind observations are needed to completely understand the formation mechanism of PMC fronts.

Declaration of competing interest

The authors declare that they have no known competing financial interests or personal relationships that could have appeared to influence the work reported in this paper.

Acknowledgement

This work was partly supported by the NASA/AIM mission under contract NAS5-03132.The authors acknowledge the efforts of the AIM and SABER data processing and science teams, and the NOGAPS–ALPHA team.

References

Bailey, S.M., Thomas, G.E., Rusch, D.W., Merkel, A.W., Jeppesen, C., Carstens, J.N., Randall, C.E., McClintock, W.E., Russell III, J.M., 2009. Phase functions of polar mesospheric cloud ice as observed by the CIPS instrument on the AIM satellite. J. Atmos. Sol. Terr. Phys. 71, 373–380. https://doi.org/10.1016/j.jastp.2008.09.039.

Benze, S., Randall, C.E., Deland, M.T., Thomas, G.E., Rusch, D.W., Bailey, S.M., Russell III, J.M., McClintock, W., Merkel, A.W., Jeppesen, C., 2009. Comparison of polar mesospheric cloud measurements from the cloud imaging and particle size experiment and the solar backscatter ultraviolet instrument in 2007. J. Atmos. Sol. Terr. Phys. 71, 365–372. https://doi.org/10.1016/j.jastp.2008.07.014.

Benze, S., Randall, C.E., DeLand, M.T., Thomas, G.E., Bailey, S.M., Russell, J.M., Merkel, A.W., 2011. Evaluation of AIM CIPS measurements of polar mesospheric clouds by comparison with SBUV data. J. Atmos. Sol. Terr. Phys. 73 (14–15), 2065–2072. https://doi.org/10.1016/j.jastp.2011.02.003.

Brown, L.B., Gerrard, A.J., Meriwether, J.W., Makela, J.J., 2004. All-sky imaging observations of mesospheric fronts in OI 557.7 nm and broadband OH airglow emissions: analysis of frontal structure, atmospheric background conditions, and potential sourcing mechanisms. J. Geophys. Res. 109, D19104. https://doi.org/10.1029/2003JD004223.

Chandran, A., Rusch, D.W., Palo, S.E., Thomas, G.E., Taylor, M.J., 2009. Gravity wave observations in the summertime polar mesosphere from the cloud imaging and particle size (CIPS) experiment on the AIM spacecraft. J. Atmos. Sol. Terr. Phys. 71 (3–4), 392–400. https://doi.org/10.1016/j.jastp.2008.09.041.

Chandran, A., et al., 2010. Polar mesospheric cloud structures observed from the cloud imaging and particle size experiment on the aeronomy of ice in the mesosphere spacecraft: atmospheric gravity waves as drivers for longitudinal variability in polar mesospheric cloud occurrence. J. Geophys. Res. 115, D13102. https://doi.org/10.1029/2009JD013185.

Chandran, A., Rusch, D.W., Thomas, G.E., Palo, S.E., Baumgarten, G., Jensen, E.J., Merkel, A.W., 2012. Atmospheric gravity wave effects on polar mesospheric clouds: a comparison of numerical simulations from CARMA 2D with AIM observations. J. Geophys. Res. 117 (D20), D20104. https://doi.org/10.1029/2012JD017794.

Dalin, P., Kirkwood, S., Moström, A., Stebel, K., Hoffmann, P., Singer, W., 2004. A case study of gravity waves in noctilucent clouds. Ann. Geophys. 22, 1875–1884. https://doi.org/10.5194/angeo-22-1875-2004.

Dalin, P., et al., 2013. First common volume ground-based and space-based measurements of the mesospheric front in noctilucent clouds. Geophys. Res. Lett. 40, 1–6. https://doi.org/10.1002/2013GL058553.

Dalin, P., et al., 2015. Evidence of the formation of noctilucent clouds due to propagation of an isolated gravity wave caused by a tropospheric occluded front. Geophys. Res. Lett. 42, 2037–2046. https://doi.org/10.1002/2014GL062776.

Dalin, P., et al., 2016. A case study of long gravity wave crests in noctilucent clouds and their origin in the upper tropospheric jet stream. J. Geophys. Res. Atmos. 121, 14,102–14,116. https://doi.org/10.1002/2016JD025422.

Dalin, P., Perminov, V., Pertsev, N., Romejko, V., 2020. Updated long-term trends in mesopause temperature, airglow emissions, and noctilucent clouds. J. Geophys. Res. Atmos. 124 https://doi.org/10.1029/2019JD030814.

Dewan, E., Picard, R., 1998. Mesospheric bores. J. Geophys. Res. 103, 6295–6305.

Dewan, E., Picard, R., 2001. On the origin of mesospheric bores. J. Geophys. Res. 106, 2921–2927.

Dubietis, A., et al., 2011. Noctilucent clouds: modern ground-based photographic observations by a digital camera network. Appl. Opt. 50 (28), F72–F79. https://doi.org/10.1364/AO.50.000F72.

Eckermann, S.D., Marks, C.J., 1997. GROGRAT: a new model of the global propagation and dissipation of atmospheric gravity waves. Adv. Space Res. 20, 1253–1256.

Eckermann, S.D., Hoppel, K.W., Coy, L., McCormack, J.P., Siskind, D.E., Nielsen, K., Kochenash, A., Stevens, M.H., Englert, C.R., 2009. High altitude data assimilation system experiments for the northern hemisphere summer mesosphere season of 2007. J. Atmos. Sol. Terr. Phys. 71, 531–551.

Ern, M., Preusse, P., Gille, J.C., Hepplewhite, C.L., Mlynczak, M.G., Russell III, J.M., M Riese, M., 2011. Implications for atmospheric dynamics derived from global observations of gravity wave momentum flux in stratosphere and mesosphere. J. Geophys. Res. 116, D19107. https://doi.org/10.1029/2011JD015821.

Ern, M., Trinh, Q.T., Preusse, P., Gille, J.C., Mlynczak, M.G., Russell III, J.M., Riese, M., 2018. GRACILE: a comprehensive climatology of atmospheric gravity wave parameters based on satellite limb soundings. Earth Syst. Sci. Data 10, 857–892. https://doi.org/10.5194/essd-10-857-2018.

France, J.A., Randall, C.E., Lieberman, R.S., Harvey, V.L., Siskind, D.E., Lumpe, J., Bailey, S.M., Carstens, J., Eckermann, S.D., Russell III, J.M., 2018. Local and remote planetary wave effects on polar mesospheric clouds in the Northern Hemisphere in 2014. J. Geophys. Res. Atmos. 123, 5149–5162. https://doi.org/10.1029/2017JD028224.

Fritts, D.C., Alexander, M.J., 2003. Gravity wave dynamics and effects in the middle atmosphere. Rev. Geophys. 41 (1), 1003. https://doi.org/10.1029/2001RG000106.

Fritts, D.C., Laughman, B., Wang, L., Lund, T.S., Collins, R.L., 2018. Gravity wave dynamics in a mesospheric inversion layer: 1. Reflection, trapping, and instability dynamics. J. Geophys. Res. Atmos. 123, 626–648. https://doi.org/10.1002/2017JD027440.

Fritts, D.C., Kaifler, N., Kaifler, B., Geach, C., Kjellstrand, C.B., Williams, B.P., et al., 2020. Mesospheric bore evolution and instability dynamics observed in PMC Turbo imaging and Rayleigh Lidar profiling over Northeastern Canada on 13 July 2018. J. Geophys. Res. Atmos. 125, e2019JD032037 https://doi.org/10.1029/2019JD032037.

Gadsden, M., Schröder, W., 1989. Noctilucent Clouds. Springer, New York, p. 165.

Gerrard, A.J., Kane, T.J., Eckermann, S.D., Thayer, J.P., 2004. Gravity waves and mesospheric clouds in the summer middle atmosphere: a comparison of lidar measurements and ray modeling of gravity waves over Sondrestrom, Greenland. J. Geophys. Res. 109, D10103. https://doi.org/10.1029/2002JD002783.

Hoffmann, L., Xue, X., Alexander, M.J., 2013. A global view of stratospheric gravity wave hotspots located with Atmospheric Infrared Sounder observations. J. Geophys. Res. Atmos. 118, 416–434. https://doi.org/10.1029/2012JD018658.

Hoppel, K.W., Baker, N.L., Coy, L., Eckermann, S.D., McCormack, J.P., Nedoluha, G.E., Siskind, D.E., 2008. Assimilation of stratospheric and mesospheric temperatures from MLS and SABER in a global NWP model. Atmos. Chem. Phys. 8, 6103–6116.

Hozumi, Y., Saito, A., Sakanoi, T., Yamazaki, A., Hosokawa, K., 2018. Mesospheric bores at southern midlatitudes observed by ISS-IMAP/VISI: a first report of an undulating wave front. Atmos. Chem. Phys. 18, 16399–16407. https://doi.org/10.5194/acp-18-16399-2018.

Kalisch, S., Preusse, P., Ern, M., Eckermann, S.D., Riese, M., 2014. Differences in gravity wave drag between realistic oblique and assumed vertical propagation. J. Geophys. Res. Atmos. 119, 10,081–10,099. https://doi.org/10.1002/2014JD021779.

Karlsson, B., Randall, C.E., Benze, S., Mills, M., Harvey, V.L., Bailey, S.M., Russell III, J. M., 2009. Intra-seasonal variability of polar mesospheric clouds due to inter-hemispheric coupling. Geophys. Res. Lett. 36, L20802 https://doi.org/10.1029/2009GL040348.

Lumpe, J.D., et al., 2013. Retrieval of polar mesospheric cloud properties from CIPS: algorithm description, error analysis and cloud detection sensitivity. J. Atmos. Sol. Terr. Phys. 104, 167–196. https://doi.org/10.1016/j.jastp.2013.06.007.

Marks, C.J., Eckermann, S.D., 1995. A three-dimensional non hydrostatic ray-tracing model for gravity waves: formulation and preliminary results for the middle atmosphere. J. Atmos. Sci. 52, 1959–1984.

McClintock, W., et al., 2009. The cloud imaging and particle size experiment on the aeronomy of ice in the mesosphere mission: instrument concept, design, calibration, and on-orbit performance. J. Atmos. Sol. Terr. Phys. 71 https://doi.org/10.1016/j.jastp.2008.10.011.

Megner, L., Stegman, J., Pautet, P.-D., Taylor, M.J., 2018. First observed temporal development of a noctilucent cloud ice void. Geophys. Res. Lett. 45, 10,003–10,010. https://doi.org/10.1029/2018GL078501.

O'Sullivan, D., Dunkerton, T.J., 1995. Generation of inertia gravity waves in a simulated life cycle of a baroclinic instability. J. Atmos. Sci. 52, 3695–3716.

Pautet, P.-D., Taylor, M.J., Snively, J.B., Solorio, C., 2018. Unexpected occurrence of mesospheric frontal gravity wave events over South Pole (90°S). Journal of Geophysical Research:Atmospheres 123, 160–173. https://doi.org/10.1002/2017JD027046.

Phillips, T., 2019. Low Latitude Noctilucent Clouds. Spaceweather.com news. https://spaceweatherarchive.com/2019/06/17/low-latitude-noctilucent-clouds/.

Preusse, P., Schroeder, S., Hoffmann, L., Ern, M., Friedl-Vallon, F., Oelhaf, H., Fischer, H., Riese, M., 2009. New perspectives on gravity wave remote sensing by spaceborne infrared limb imaging. Atmos. Meas. Tech. 2, 299–311.

Remsberg, et al., 2008. Assessment of the quality of the Version 1.07 temperature versus-pressure profiles of the middle atmosphere from TIMED/SABER. J. Geophys. Res. 113, D17101. https://doi.org/10.1029/2008JD010013.

Rong, P.P., Russell III, J.M., Hervig, M.E., Bailey, S.M., 2012. The roles of temperature and water vapor at different stages of the polar mesospheric cloud season. J. Geophys. Res. 117, D04208 https://doi.org/10.1029/2011JD016464.

Rong, P.P., Russell III, J.M., Marshall, B.T., Gordley, L.L., Mlynczak, M., Walker, K., 2019. Validation of water vapor measured by SABER on the TIMED satellite. J. Atmos. Sol. Terr. Phys. https://doi.org/10.1016/j.jastp.2019.105099.

Rusch, D.W., et al., 2009. The cloud imaging and particle size experiment on the aeronomy of ice in the mesosphere mission: cloud morphology for the northern 2007 season. J. Atmos. Sol. Terr. Phys. 71, 356–364. https://doi.org/10.1016/j.jastp.2008.11.005.

Russell III., J.M., Mlynczak, M.G., , M. G., Gordley, L.L., Tansock, J., Esplin, R., 1999. An overview of the SABER experiment and preliminary calibration results. Proceedings of the SPIE, 44th Annual Meeting 3756, 277–288. Denver, Colo., 18–23 July.

Russell III, J.M., et al., 2009. Aeronomy of ice in the mesosphere (AIM): overview and early science results. J. Atmos. Sol. Terr. Phys. https://doi.org/10.1016/j.jastp.2008.08.011.

Russell III, J.M., Rong, P., Hervig, M.E., Siskind, D.E., Stevens, M.H., Bailey, S.M., Gumbel, J., 2014. Analysis of northern midlatitude noctilucent cloud occurrences using satellite data and modeling. J. Geophys. Res. Atmos. 119, 3238–3250. https://doi.org/10.1002/2013JD021017.

She, C.Y., Li, T., Williams, B.P., Yuan, T., Picard, R.H., 2004. Concurrent OH imager and sodium temperature/wind lidar observation of a mesopause region undular bore event over Fort Collins/Platteville, Colorado. J. Geophys. Res. 109, 22107–22115. https://doi.org/10.1029/2004JD004742.

Simkhada, D.B., Snively, J.B., Taylor, M.J., Franke, S.J., 2009. Analysis and modeling of ducted and evanescent gravity waves observed in the Hawaiian airglow. Ann. Geophys. 27, 3213–3224. https://doi.org/10.5194/angeo-27-3213-2009.

Smith, S.M., 2014. The identification of mesospheric frontal gravity-wave events at a mid-latitude site. Adv. Space Res. 54, 417–424.

Smith, S.M., Friedman, J., Raizada, S., Tepley, C., Baumgardner, J., Mendillo, M., 2005. Evidence of mesospheric bore formation from a breaking gravity wave event: simultaneous imaging and lidar measurements. J. Atmos. Sol. Terr. Phys. 67, 345–356.

Solodovnik, A.A., Leontyev, P.I., Dalin, P., 2020. Studies of the influence of tropospheric factors on the formation of noctilucent clouds by a cartographic method. J. Atmos. Sol. Terr. Phys. https://doi.org/10.1016/j.jastp.2020.105224.

Stevens, M.H., Englert, C.R., Hervig, M.E., Petelina, S.V., Singer, W., Nielsen, K., 2009. The diurnal variation of polar mesospheric cloud frequency near 55oN observed by SHIMMER. J. Atmos. Sol. Terr. Phys. 71, 401–407.

Stevens, M.H., Lieberman, R.S., Siskind, D.E., McCormack, J.P., Hervig, M.E., Englert, C. R., 2017. Periodicities of polar mesospheric clouds inferred from a meteorological analysis and forecast system. J. Geophys. Res. Atmos. 122, 4508–4527. https://doi.org/10.1002/2016JD025349.

Swenson, G.R., Espy, P.J., 1995. Observations of 2-dimensional airglow structure and Na density from the ALOHA, October 9, 1993 'storm flight'. Geophys. Res. Lett. 22, 2845–2848.

Taylor, M.J., Turnbull, D.N., Lowe, R.P., 1995. Spectrometric and imaging measurements of a spectacular gravity wave event observed during the ALOHA-93 campaign. Geophys. Res. Lett. 22 (20), 2849–2852.

Thomas, G.E., 2003. Are noctilucent clouds harbingers of global change in the middle atmosphere? Adv. Space Res. 32 (9), 1737–1746.

Thurairajah, B., et al., 2013. Morphology of polar mesospheric clouds as seen from space. J. Atmos. Sol. Terr. Phys. https://doi.org/10.1016/j.jastp.2012.09.009.

Thurairajah, B., Siskind, D.E., Bailey, S.M., Carstens, J.N., Russell III, J.M., Mlynczak, M. G., 2017. Oblique propagation of monsoon gravity waves during the northern hemisphere 2007 summer. J. Geophys. Res. Atmos. 122, 5063–5075. https://doi.org/10.1002/2016JD026008.

Thurairajah, B., Cullens, C.Y., Siskind, D.E., Hervig, M.E., Bailey, S.M., 2020. The role of vertically and obliquely propagating gravity waves in influencing the polar summer mesosphere. J. Geophys. Res. Atmos. 125, e2020JD032495 https://doi.org/10.1029/2020JD032495.

von Zahn, U., 2003. Are noctilucent clouds truly a "miner's canary'' of global change? EOS Trans. AGU 84 (28), 261.

Wilms, H., Rapp, M., Hoffmann, P., Fiedler, J., Baumgarten, G., 2013. Gravity wave influence on NLC: experimental results from ALOMAR, 69°N. Atmos. Chem. Phys. 13, 11,951–11,963. https://doi.org/10.5194/acp-13-11951-2013.

Yamashita, C., England, S.L., Immel, T.J., Chang, L.C., 2013. Gravity wave variations during elevated stratopause events using SABER observations. J. Geophys. Res. Atmos. 118 https://doi.org/10.1002/jgrd.50474.

Yue, J., She, C.-Y., Nakamura, T., Harrell, S., Yuan, T., 2010. Mesospheric bore formation from large-scale gravity wave perturbations observed by collocated all-sky OH imager and sodium lidar. J. Atmos. Sol. Terr. Phys. 72, 7–18.

Yue, J., Thurairajah, B., Hoffmann, L., Alexander, J., Chandran, A., Taylor, M.J., Russell III, J.M., Randall, C.E., Bailey, S.M., 2014. Concentric gravity waves in polar mesospheric clouds from the Cloud Imaging and Particle Size experiment. J. Geophys. Res. Atmos. 119, 5115–5127. https://doi.org/10.1002/2013JD021385.

Zhao, Y., et al., 2015. Investigating seasonal gravity wave activity in the summer polar mesosphere. J. Atmos. Sol. Terr. Phys. 127, 8–20. https://doi.org/10.1016/j.jastp.2015.03.008.